Complex Permittivity Reconstruction Using Skin Surface Reflection and Neural Network for Microwave Breast Imaging

Peixian Zhu, *Graduate Student Member, IEEE*, and Shouhei Kidera, *Senior Member, IEEE*

***Abstract*—This study introduces an experimental validation for the complex permittivity profile reconstruction using the multilayer perceptron (MLP) neural network (NN) approach for quantitative microwave recognition of breast cancer. A direct conversion from the four-dimensional scattered data to the complex permittivity three-dimensional profile can be achieved by combining the MLP-NN and the skin surface rejection preprocessing. The experimental data, measured by ultra-wideband radar equipment using a simplified breast phantom, validates that our approach provides both the real and imaginary parts of complex permittivity profiles, even when using limited numbers of training datasets.**

***Index Terms*—Complex permittivity reconstruction, deep neural network (DNN), Microwave breast cancer detection, skin surface rejection (SSR), ultra-wideband (UWB) radar.**

I. Introduction

BREAST cancer is one of the most fatal and diagnosed cancers in worldwide [1]. The X-ray mammography, which is a current major diagnostic modality, has several disadvantages and can cause harm via exposure of healthy tissues to X-rays and painful compression during measurement. By contrast, the microwave-based screening modality can achieve low cost, harmless, and painless measurement, which contributes to more frequent screening, and thereby improves the early detection rate of breast cancer. A large-scale study of the dielectric characterization of breast tissues revealed significant differences in the complex permittivity between cancerous and normal adipose tissues in microwave frequency bands [2]. These findings accelerated recent research focused on microwave mammography.

The confocal imaging method, or radar approach, is a current major imaging scheme that has been introduced in numerous studies [3], [4]. However, because of the low dielectric contrast between cancer and fibro-glandular tissues, detecting cancer particular in dense breast media, remains difficult, causing a high false-positive rate. In contrast to the radar approach, the tomographic approach (or inverse scatter analysis) can provide a quantitative estimate of the complex permittivity profile by solving the domain integration equation [5], [6]. However, the three-dimensional (3D) reconstruction using an inverse scattering scheme, is quite challenging, because the number of unknowns is much larger than that of the data sample, namely, ill-posed condition. Several studies have assessed the quantitative profile reconstruction of both permittivity and conductivity, using a real microwave radar module for breast cancer detection.

To overcome the above difficulty, machine learning is being increasingly used to recognize cancers via the use of microwave scattered data. A support vector machine (SVM) classifier has been introduced to identify the nature of the tumor, where the radar data of the 3D breast cancer model were used as input data [7]. Clinical microwave mammography data has been validated via the SVM classifier with a secondary kernel to detect the breast lesion [8]. Furthermore, a convolutional neural network (NN) was introduced to diagnose cancer using large-scale dataset, giving a 80% recognition accuracy [9], or other deep learning scheme [10]. However, these machine learning approaches have inherent problems, where the recognition accuracy is highly dependent of the selected training datasets, while a quantitative value of complex permittivity is hardly available from the outputs. In addition, the above mentioned studies did not consider the effect of skin surface reflections adequately.

Accordingly, the current study presents a 3D quantitative imaging for a complex permittivity profile, using a multiple layer perceptron (MLP) NN model, where the four-dimensional (4D) scattered data (transmitter, receiver, frequency, and rotation angle) are directly associated with the spatial profile of a simplified phantom. In addition, this scheme introduces preprocessing for SSR because the reflection responses include a skin reflection that is much larger than that from inner tissues, $i.e.$, cancer. Moreover, to the best of our knowledge, there are only few studies that have incorporated both the SSR and machine learning. Numerous SSR approaches exist, including a finite impulse response filter [4], singular value decomposition [11], entropy-based time window [12], or two-stage processing [13]. Among these, this study selected one of the most effective rejection schemes based on the fractional derivative (FD) model [14]. A notable feature of the FD-based SSR is the compensation for the frequency-dependent waveform deformation, caused by the mutual coupling between the antenna and skin tissue, by optimizing the FD parameters. While the SSR scheme has been

Manuscript received 28 April 2023; revised 11 July 2023 and 1 September 2023; accepted 20 September 2023. Date of publication 16 October 2023; date of current version 22 November 2023. This work was supported by Japan Society for the Promotion of Science under Grant JP20H02161. *(Corresponding author: Peixian Zhu.)*

The authors are with the Graduate School of Informatics and Engineering, The University of Electro-Communications, Tokyo 182-8585, Japan (e-mail: zhu.peixian@ems.cei.uec.ac.jp; kidera@uec.ac.jp).

Digital Object Identifier 10.1109/JERM.2023.3321423

2469-7249 © 2023 IEEE. Personal use is permitted, but republication/redistribution requires IEEE permission.
See https://www.ieee.org/publications/rights/index.html for more information.

Authorized licensed use limited to: UNIVERSITY OF ELECTRO COMMUNICATIONS. Downloaded on May 23,2025 at 13:13:21 UTC from IEEE Xplore. Restrictions apply.

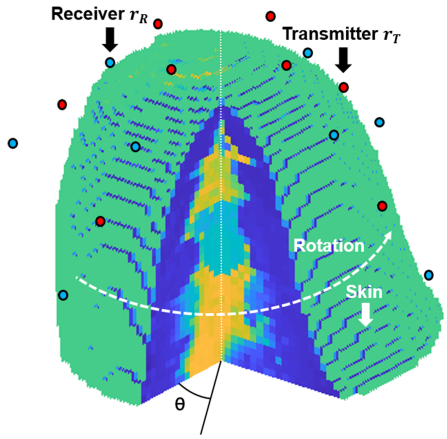

Fig. 1. Observation model.

demonstrated in radar imaging scenario as [15], there are quite few studies to combine the SSR and the machine learning schemes.

The main contribution of this study is summarized below:

1) The effective SSR method, known as SSR-FD, significantly improves the reconstruction accuracy of complex permittivity in MLP-NN-based complex permittivity estimations.
2) Our proposed scheme, validated experimentally using several simplified breast phantoms accurately reconstructs the relative permittivity and conductivity of each type of breast tissues ($i.e.$, adipose, fibro-glandular, skin, and three types of cancer).

II. Method

A. Observation Model

The observation model is shown in Fig. 1. Multiple transmitters and receivers were configured in arrays, which were rotated along the z axis. $S(\mathbf{r}_T, \mathbf{r}_R, \omega, \theta)$ denotes the scattered electric field from the transmitter $\mathbf{r}_T$ to the receiver $\mathbf{r}_R$ with the frequency ω at the rotation angle θ.

B. Skin Surface Rejection (SSR) Preprocessing

The reflection from the skin surface is a dominant clutter in reflection responses, and an incomplete suppression of this component incurs a serious inaccuracy for postimaging or recognition process, such as radar imaging or NN-based machine learning. To remove the skin reflection signal, we introduce two SSR schemes. Here, we prepared the reference signal, including only skin and low contrast adipose tissues, which is denoted as $s^{\mathrm{ref}}(\mathbf{r}_T, \mathbf{r}_R, \theta; t)$. If the distance between the skin and antenna is kept constant when rotating the array, the following averaging operation would enhance the signal-to-noise ratio as:

$$\bar{s}^{\mathrm{ref}}(\mathbf{r}_T, \mathbf{r}_R; t) = \frac{1}{N_\theta} \sum_{i=1}^{N_\theta} s^{\mathrm{ref}}(\mathbf{r}_T, \mathbf{r}_R, \theta_i; t) \tag{1}$$

where θ_i denotes the i-th rotation angle and N_θ is the total number of sampled rotation angles.

1) SSR-AVE: First, we introduce the simple SSR scheme, known as SSR-AVE, which adjusts the time delay and amplitude from the above-mentioned reference response $\bar{s}^{\mathrm{ref}}(\mathbf{r}_T, \mathbf{r}_R; t)$ Then, the clutter suppressed signal with the SSR-AVE $\tilde{s}_{\mathrm{AVE}}(t)$ is formed as:

$$\begin{aligned}&\tilde{s}_{\mathrm{AVE}}(\mathbf{r}_T, \mathbf{r}_R, \theta; t)\\ &= s(\mathbf{r}_T, \mathbf{r}_R, \theta; t) - \hat{A}\bar{s}^{\mathrm{ref}}(\mathbf{r}_T, \mathbf{r}_R; t - \hat{\tau})\end{aligned} \tag{2}$$

where $\hat{A}$ and $\hat{\tau}$ are determined as:

$$\begin{aligned}&(\hat{A}, \hat{\tau})\\ &= \underset{A,\tau}{\mathrm{argmin}} \int_{T_{\mathrm{r}}}^{T_{\mathrm{r}}+T_{\mathrm{W}}} \left| s(\mathbf{r}_T, \mathbf{r}_R, \theta; t) - \hat{A}\bar{s}^{\mathrm{ref}}(\mathbf{r}_T, \mathbf{r}_R; t - \hat{\tau}) \right|^2 dt\end{aligned} \tag{3}$$

Here, T_{r} represents the rise time of $S(\mathbf{r}_T, \mathbf{r}_R, \theta; t)$, while T_{W} signifies the temporal window length. This length is determined by considering the effective pulse width of the transmitted signal, as the skin surface reflection occurs within this pulse width from the rise time as T_{r}. As outlined in [14], if T_{W} is smaller or larger than an effective pulse width, it would result in insufficient or over-suppression, meaning that the responses from fibroglandular or cancer cells could be suppressed as well.

2) SSR-FD: While the SSR-AVE suppresses the SSR at a certain level, this could not compensate for the deformation due to frequency-dependent scattering effects, which are mainly caused by the mutual coupling between the skin and antenna or by other near-field effects. Thus, the method introduces FD-based waveform compensation [14] using an additional parameter α. In this method, the skin surface response is formed as:

$$\tilde{s}_{\mathrm{ref}}(\mathbf{r}_T, \mathbf{r}_R; t; \alpha) = \mathcal{F}^{-1}[(j\omega)^\alpha \bar{S}^{\mathrm{ref}}(\mathbf{r}_T, \mathbf{r}_R; \omega)] \tag{4}$$

where $\bar{S}^{\mathrm{ref}}(\mathbf{r}_T, \mathbf{r}_R; \omega) = \mathcal{F}[\bar{s}^{\mathrm{ref}}(\mathbf{r}_T, \mathbf{r}_R; t)]$, and $\mathcal{F}$ denotes the Fourier transform, $(j\omega)^\alpha$ denotes the FD operator; in particular, $\alpha = 1$, $\tilde{s}(\mathbf{r}_T, \mathbf{r}_R; t; \hat{\alpha})$ expresses the time derivative waveform of $\bar{s}_{ref}(t)$. Then, the clutter-eliminated signal by the SSR-FD denoted $\tilde{s}_{\mathrm{FD}}(t)$ is formed as:

$$\tilde{s}_{\mathrm{FD}}(t) = s(\mathbf{r}_T, \mathbf{r}_R, \theta; t) - \hat{A}\bar{s}^{\mathrm{ref}}(\mathbf{r}_T, \mathbf{r}_R; t - \hat{\tau}; \hat{\alpha}) \tag{5}$$

where $\hat{A}$, $\hat{\tau}$, and $\hat{\alpha}$ are optimized as follows:

$$\begin{aligned}&(\hat{A}, \hat{\tau}, \hat{\alpha})\\ &= \underset{A,\tau,\alpha}{\mathrm{argmin}} \int_{T_{\mathrm{r}}}^{T_{\mathrm{r}}+T_{\mathrm{W}}} \left| s(\mathbf{r}_T, \mathbf{r}_R, \theta; t) - \hat{A}\tilde{s}_{\mathrm{ref}}(\mathbf{r}_T, \mathbf{r}_R; t - \hat{\tau}; \hat{\alpha}) \right|^2 dt\end{aligned} \tag{6}$$

Several studies, including [14], demonstrated that the SSR-FD method significantly upgrades the suppression performance in various types of observation and target models.

C. MLP-Based Conversion Method

As described above, numerous studies have assessed quantitative imaging using inverse scattering analysis; however, these

Authorized licensed use limited to: UNIVERSITY OF ELECTRO COMMUNICATIONS. Downloaded on May 23,2025 at 13:13:21 UTC from IEEE Xplore. Restrictions apply.

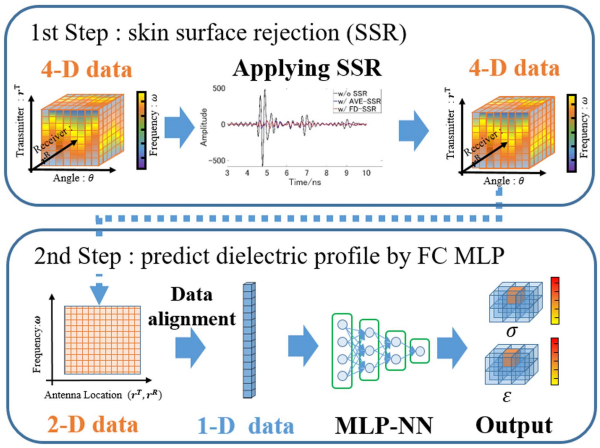

Fig. 2. Schematic diagram of the proposed method for 3-D complex permittivity reconstruction.

approaches suffer from substantial limitations for inaccuracy or experimental computational cost due to ill-posed or nonlinear optimization problem. This study introduces a direct conversion scheme from scattered data to 3-D complex permittivity profile via the NN scheme. Fig. 2 shows the fully connected NN structure that converts the complex-valued frequency response data to the dielectric properties located at the 3D voxel. Here, the 4D scattered data in terms of transmitter, receiver frequency, and rotation angle, are aligned to the following one-dimensional input vector $\boldsymbol{X}$:

$$\begin{aligned}\boldsymbol{X} \equiv [&\xi_{1,1,1,1},\ldots,\xi_{1,1,1,l},\xi_{1,1,2,1},\ldots,\xi_{1,1,2,l},\ldots,\\ &\xi_{1,1,k,1},\ldots,\xi_{1,1,k,l},\xi_{1,2,1,1},\ldots,\xi_{1,2,1,l},\xi_{1,2,2,1},\ldots,\\ &\xi_{1,2,2,l},\ldots,\xi_{1,2,k,1},\ldots,\xi_{1,j,k,l},\ldots,\xi_{i,1,1,1},\ldots,\xi_{i,1,1,l},\\ &\xi_{i,1,2,1},\ldots,\xi_{i,1,2,l},\ldots,\xi_{i,1,k,1},\ldots,\xi_{i,j,k,l}]\end{aligned} \tag{7}$$

Here, $\xi_{i,j,k,l}$ is defined as:

$$\xi_{i,j,k,l} \equiv S\left(\mathbf{r}_i^{\mathrm{T}}, \mathbf{r}_j^{\mathrm{R}}, \omega_k, \theta_l\right) \tag{8}$$

$S(\mathbf{r}_i^{\mathrm{T}}, \mathbf{r}_j^{\mathrm{R}}, \omega_k, \theta_l)$ denotes the scattered data from the i-th transmitter to the j-th receiver at the k-th angular frequency at l-th angle, which is obtained with or without SSR pre-processing.

In this case, the 3D breast area is divided into several cube cells, namely, $N \times M \times L$, along the x, y, and z axis, respectively, to reduce the reconstruction unknowns. Each cube cell has a variable for relative permittivity ϵ and the conductivity σ. The output vector $\mathbf{Y}$ is defined as:

$$\boldsymbol{Y} \equiv [\boldsymbol{y}_{1,1,1},\ldots,\boldsymbol{y}_{1,1,l},\boldsymbol{y}_{1,2,1},\ldots,\boldsymbol{y}_{1,m,l},\ldots,\boldsymbol{y}_{n,m,l},] \tag{9}$$

where $\mathbf{y}_{n,m,l}$ is defined as:

$$\boldsymbol{y}_{n,m,l} \equiv [\boldsymbol{\epsilon}_{n,m,l}, \boldsymbol{\sigma}_{n,m,l}] \tag{10}$$

(a) Top view of phantom. (b) Side view of radar and phantom.

Fig. 3. Experimental setup for UWB radar and simplified breast phantom.

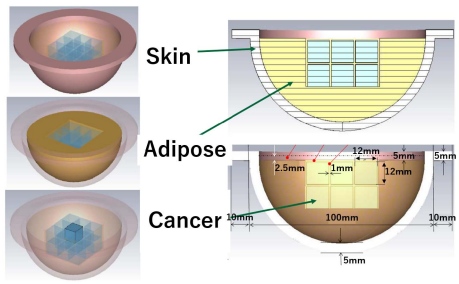

Fig. 4. 3-D structure of simplified breast phantom. Central 18 cubes are exchangeable in terms of adipose, fibro-glandular, and cancer mimicking dielectric cells.

These parameters are then converted to the complex permittivity at the specific angular frequency ω by using the equation:

$$\bar{\boldsymbol{\epsilon}}_{n,m,l}(\omega) = \boldsymbol{\epsilon}_{n,m,l} - i\frac{\boldsymbol{\sigma}_{n,m,l}}{\epsilon_0 \omega} \tag{11}$$

Here, ϵ_0 denotes the permittivity of free space.

III. Results

A. Experimental Setup

We introduce the experimental validations using a simplified breast phantom. The experimental setp using the UWB radar module and the phantom is shown in Fig. 3. The handheld type UWB radar module, which was developed in [16] and was provided by Prof. Kikkawa's research group at Hiroshima University. The frequency band of this module is from 3.1 to 10.0 GHz. The module constitutes an array of eight transmitters and eight receivers on the circumference of a hemi-sphere with 75-mm radius that can be rotated 360°, where the distance between the module and the phantom should be minimized. In this case, 16 combinations of transmitters and receivers and 40 samples along rotation angles were set to observation points. Five frequencies from 3.0 to 7.0 GHz with 1.0 GHz intervals were used for all experiments. The simplified breast phantoms are shown in Fig. 4, where 18 cubic cells with 12 mm dimension are buried into the central position of the phantom. Then, $N = 3$, $M = 3$, and $L = 2$, are set. The skin and surrounding adipose media were represented by solid or semi-solid material. To generate a large number of patterns, we introduced five types of

Authorized licensed use limited to: UNIVERSITY OF ELECTRO COMMUNICATIONS. Downloaded on May 23,2025 at 13:13:21 UTC from IEEE Xplore. Restrictions apply.

TABLE I
DIELECTRIC PARAMETERS FOR EACH TISSUE CELL

Tissue (State).	Relative permittivity.	Conductivity [S/m].
Adipose (Liquid).	3.4	0.06
Adipose (semi-solid).	3.6	0.09
Skin.	22.84	0.97
Mammary gland.	22.84	0.97
Cancer type 1.	27.51	1.07
Cancer type 2.	46.63	2.04
Cancer type 3.	32.05	1.56

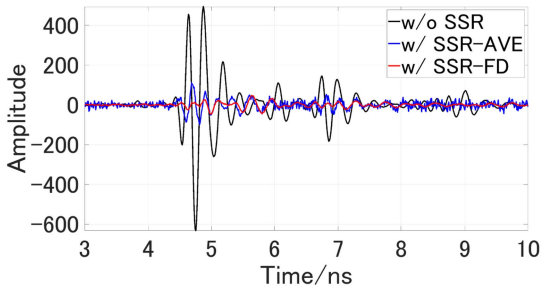

Fig. 5. Comparison of time-domain response with or without applying SSR scheme.

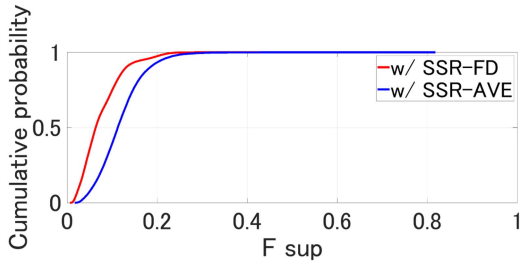

Fig. 6. Cumulative probability of $\mathrm{F_{sup}}$ in each SSR method.

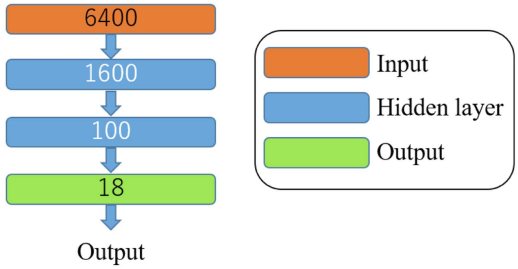

Fig. 7. Number of neurons in each layer.

cubic dielectric material, modeling the adipose, fibro-glandular, and three types (low, middle, and high dielectric property) of cancer tissues, to arrange the above 18 positions. Table I shows the dielectric property for each cubic phantom. In this case, where 66 different patters are investigated.

B. SSR Performance

First, the evaluation of the SSR performance was validated as follows. The reference signal, defined as $s^{\mathrm{ref}}(\mathbf{r}_T, \mathbf{r}_R, \theta; t)$ in (1), was allocated to when all 18 cubes were set to adipose tissues; thus, the response from inner area of the phantom would be negligible. An example for the SSR application is shown in Fig. 5, which demonstrates that both the SSR-AVE and SSR-FD can suppress the skin surface response at the earliest time of arrival. Moreover, the SSR-FD offers more suppression than the SSR-AVE does, which indicates that the FD-based waveform compensation was also effective in this case. To assess the suppression performance of each method, the following criteria are defined as:

$$F_{\mathrm{sup}} = \frac{\max_{T_{\mathrm{r}}<t<T_{\mathrm{r+W}}} \tilde{s}_{\mathrm{woSSR}}(t)}{\max_{T_{\mathrm{r}}<t<T_{\mathrm{r+W}}} \tilde{s}_{\mathrm{wSSR}}(t)} \tag{12}$$

where $\tilde{\mathrm{s}}_{\mathrm{woSSR}}(t)$ and $\tilde{\mathrm{s}}_{\mathrm{wSSR}}(\mathrm{t})$ denote the scattered response without and with SSR, respectively. $\mathrm{F_{sup}}$ assesses the suppression ratio from the case without SSR within the allocated time range. If the index is sufficiently small, it can be concluded that the skin surface response has been sufficiently removed. The statistical results for the SSR performance are shown in Fig. 6, indicating the histogram and cumulative distribution function of $\mathrm{F_{sup}}$ of all processed results from all 66 patterns by each SSR scheme. SSR-FD is more advantageous in terms of SSR performance.

C. Reconstruction Results

Here, the 3D reconstruction results of complex permittivity are presented. In this case, the 16 combinations of the transmitters and receivers were used, and the number of angular frequency was set to 5 (3, 4, 5, 6, and 7 GHz). As shown in Fig. 3, the array is rotated around the vertical axis. Data is acquired at 9 ° intervals from $0 \leq \theta \leq 360$ °, resulting in 40 samples along the θ direction. The two hidden layers based on the NN model shown in Fig. 7 were used. In each hidden layer, batch normalization, dropout, and fully-connected processes were applied.

We observed 66 different phantom patterns, by changing a dielectric parameter and position. In the reconstruction by the NN, the leave-one-out validation was applied; therefore, for one specific test data, we use the training data with 65 different patterns without any validation samples, in training NN. The two examples of the 3D reconstruction results, obtained by each approach are shown in Figs. 8 and 9. As can be seen from the examples, the NN with SSR-FD method shows more accurate reconstruction of the dielectric profile, in both real and imaginary parts. This is because the scattered responses from the inner breast area would be more prominent by following SSR-FD. The internal tissue structure of the breast could be reconstructed more accurately by using the simple MLP NN approach. The average computational times for SSR-FD and the NN-based reconstruction are 7 and 300 s, respectively, for each phantom pattern, using an Intel(R) Xeon(R) Gold 6330 CPU @ 2.00 GHz CPU and 1.00 TB RAM.

Finally, we introduce a quantitative error analysis using root mean square errors (RMSE). Here, the RMSEs for the real and

Authorized licensed use limited to: UNIVERSITY OF ELECTRO COMMUNICATIONS. Downloaded on May 23,2025 at 13:13:21 UTC from IEEE Xplore. Restrictions apply.

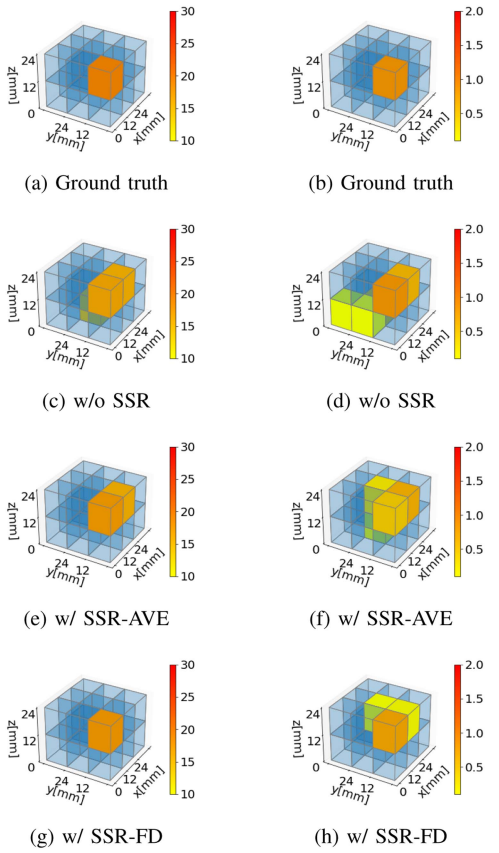

(a) Ground truth (b) Ground truth

(c) w/o SSR (d) w/o SSR

(e) w/ SSR-AVE (f) w/ SSR-AVE

(g) w/ SSR-FD (h) w/ SSR-FD

Fig. 8. These figures are reconstruction results of real part and imaginary part of profile in Pattern 1. Color denotes each value of real part and imaginary part of profile. (a) and (b) denote the ground truth profile. (c)–(h) denote the reconstruction results using each SSR scheme. 1st column: $\Re[\epsilon]$. 2nd column: $\Im[\epsilon]$.

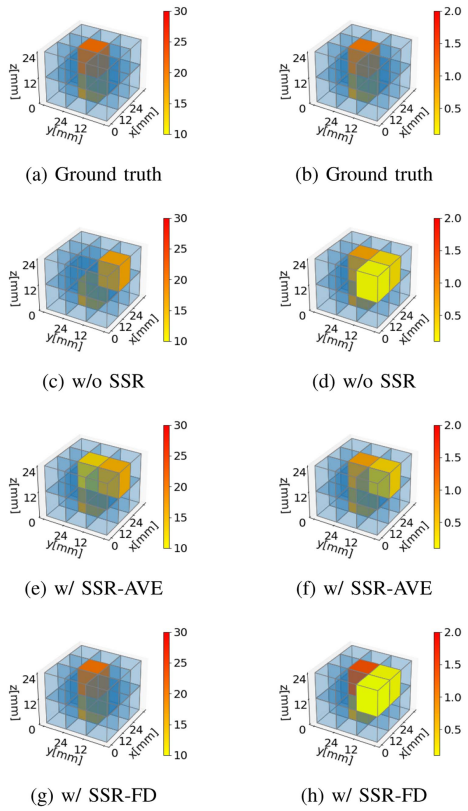

(a) Ground truth (b) Ground truth

(c) w/o SSR (d) w/o SSR

(e) w/ SSR-AVE (f) w/ SSR-AVE

(g) w/ SSR-FD (h) w/ SSR-FD

Fig. 9. These figures are reconstruction results of real part and imaginary part of profile in Pattern 2. Color denotes each value of real part and imaginary part of profile. (a) and (b) denote the ground truth profile. (c)–(h) denote the reconstruction results using each SSR scheme. 1st column: $\Re[\epsilon]$. 2nd column: $\Im[\epsilon]$.

imaginary complex permittivity are defined as:

$$\mathrm{RMSE}_{\Re[\epsilon_r]} = \sqrt{\frac{1}{K}\sum_{k=1}^{K}(\Re[\epsilon_{r,\mathrm{true}}(\boldsymbol{r}_k)] - \Re[\epsilon_r(\boldsymbol{r}_k)])^2}, \quad (13)$$

$$\mathrm{RMSE}_{\Im[\epsilon_r]} = \sqrt{\frac{1}{K}\sum_{k=1}^{K}(\Im[\epsilon_{r,\mathrm{true}}(\boldsymbol{r}_k)] - \Im[\epsilon_r(\boldsymbol{r}_k)])^2} \quad (14)$$

where $\epsilon_{\mathrm{r}}(\boldsymbol{r}_k)$ is the complex permittivity at the location of $\boldsymbol{r}_k$, corresponding k-the cube. The subscript "true" denotes the true value and K denotes the number of cells. Fig. 10 shows the boxplots of the RMSE for the real and imaginary parts of complex permittivity. Here, the MLP based training requires a random optimization scheme, and then, the obtained results depends on the selected seed of random pattern. To provide statistically meaningful results, we average each RMSE for ten different random seeds. These plots also confirm that the SSR-FD-based reconstruction attains the most accurate results in quantitative criteria.

It is noteworthy that although the SSR method eliminates most of the skin reflections, and enhances the signal characteristics of the internal tissues of the breast model, there are still some errors in the reconstructed images. These errors occur because the scattered data still include unnecessary responses from the air gap among cubic cells or the adjustment spatial errors between the radar and phantom. Moreover, employing a multi-frequency inversion scheme could also enhance the reconstruction accuracy.

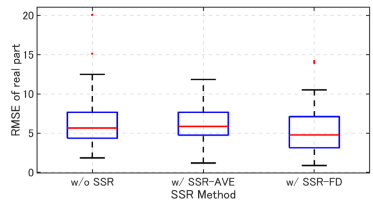

(a) RMSE of $\Re[\epsilon]$.

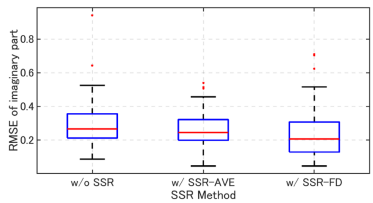

(b) RMSE of $\Im[\epsilon]$.

Fig. 10. Box plots for average of RMSE for 10 runs of real and imaginary parts of complex permittivity in 66 different patterns. Red line is median value. Box denotes the interquartile range (IQR). Whisker denotes the most extreme data points but not considered outliers.

Authorized licensed use limited to: UNIVERSITY OF ELECTRO COMMUNICATIONS. Downloaded on May 23,2025 at 13:13:21 UTC from IEEE Xplore. Restrictions apply.

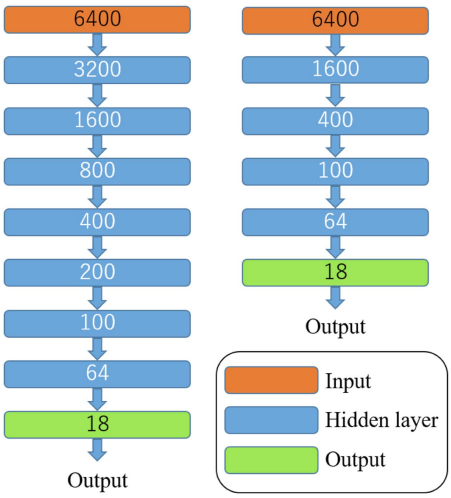

(a) Number of neurons in each layer, in terms of different numbers of hidden layers.

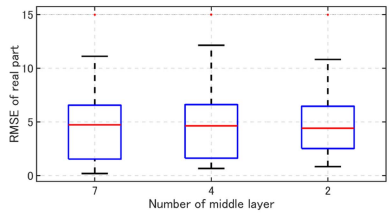

(b) RMSE of $\Re[\epsilon]$.

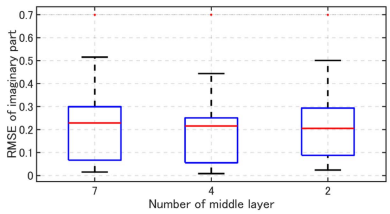

(c) RMSE of $\Im[\epsilon]$.

Fig. 11. Sensitivity analysis for number of middle layer in the proposed scheme. (a) shows structure of MLP-NN. (b) and (c) are boxplots for RMSE for different hidden layers, where the SSR-FD processing is used.

D. *Sensitivity for the Number of Hidden Layers*

Here, the sensitivity to the number of hidden layers in MLP-NN model is described. Fig. 11(a) shows the other two different settings for the number of hidden layers as four and seven hidden layers. The boxplots of the real part and imaginary part RMSE for each hidden layer model are shown in Fig. 11(b) and (c), respectively, and they demonstrate that the case with two hidden layers had the most accurate results in both real and imaginary parts of complex permittivity with SSR-FD based reconstruction. This is because a larger number of hidden layers incurs over-fitting problems, and the appropriate layer model should be selected in considering the number of training data and input vectors. Notably, the performance of the SSR or MLP-NN would vary depending on the assumed array configuration, as the distance between elements and skin surface affects the waveform deformation in skin reflection. Therefore, a crucial part of our future work involves optimizing the array configuration to improve the reconstruction accuracy.

IV. Conclusion

This study introduces a method that incorporates the effective SSR and deep NN-based 3D complex permittivity reconstruction scheme for microwave breast cancer imaging scenarios. To extract the responses from the inner area, such as cancerous tissues, we introduced an effective SSR approach based on a FD model, which compensates for the deformation due to frequency dependent scattering effects, mainly caused by the mutual coupling between the skin and antenna, or other near-field effects. In addition, to avoid a computationally expensive imaging scheme, such as inverse scattering analysis, this study introduces a direct conversion scheme from scattered data to a 3D complex permittivity profile via MLP-NN scheme. The experiment used the actual MIMO UWB radar module and simplified breast phantoms demonstrated that the SSR-FD approach provided greater suppression performance compared with that in the traditional SSR scheme. Given that there are few studies on the combination of the SSR and machine learning approach, we have primarily used the traditional SSR-AVE scheme (commonly used in [4], [11], [12], [13]) for comparison with existing works. Additionally, the MLP-NN with SSR-FD preprocessing scheme had significant advantages in that the 3D quantitative reconstruction was achieved at a certain level of accuracy in both real and imaginary parts of complex permittivity using limited sets of training data.

To further enhance the reconstruction performance by MLP-NN, a numerical simulation analysis is promising. The number of training data could be significantly increased by introducing various phantom pattern types. Several studies exist that calibrate data to interchange the simulated and experimental data, and it is within our future scope to apply such a calibration process for further clinical or practical applications. Additionally, if we enlarge our database with more phantom patterns, we will share it with an online database. Note that, as the MLP-NN-based reconstruction is a type of "black box", it does not necessarily satisfy the physical condition. Therefore, feedback with physical interpretation should be incorporated, such as through simulation-based re-evaluation or combined use of the inverse scattering scheme, as in [17]. In addition to improving the reconstruction performance of NN, we also consider improving the radar module so that it can measure transmissive signal, which is sensitive to phase shift due to changes in the relative permittivity.

Acknowledgment

The author acknowledge support from Prof. Takamaro Kikkawa at Research Institute for Nanodevice and Bio System, Hiroshima University for providing the radar equipment.

References

[1] F. Bray, J. Ferlay, I. Soerjomataram, R. Siegel, L. Torre, and A. Jemal, "Global cancer statistics 2018: GLOBOCAN estimates of incidence and mortality worldwide for 36 cancers in 185 countries," *CA, Cancer J. Clinicians*, vol. 68, no. 6, pp. 394–424, Dec. 2018.

[2] M. Lazebnik et al., "A large-scale study of the ultrawideband microwave dielectric properties of normal, benign and malignant breast tissues obtained from cancer surgeries," *Phys. Med. Biol.*, vol. 52, no. 20, pp. 2637–2656, 2007.

Authorized licensed use limited to: UNIVERSITY OF ELECTRO COMMUNICATIONS. Downloaded on May 23,2025 at 13:13:21 UTC from IEEE Xplore. Restrictions apply.

[3] T. Sugitani, S. Kubota, A. Toya, X. Xiao, and T. Kikkawa, "A compact 4×4 planar UWB antenna array for 3-D breast cancer detection," *IEEE Antennas Wireless Propag. Lett.*, vol. 12, pp. 733–736, 2013.
[4] E. J. Bond, X. Li, and S. C. Hagness, and B. D. Van Veen, "Microwave imaging via space-time beamforming for early detection of breast cancer," *IEEE Trans. Antennas Propag.*, vol. 51, no. 8, pp. 1690–1705, Aug. 2003.
[5] W. C. Chew and Y. M. Wang, "Reconstruction of two-dimensional permittivity distribution using the distorted Born iterative method," *IEEE Trans. Med. Imag.*, vol. 9, no. 2, pp. 218–225, Jun. 1990.
[6] H. Sato and S. Kidera, "Multi-frequency integration algorithm of contrast source inversion method for microwave breast tumor detection," in *Proc. IEEE Eng. Med. Biol. Conf.*, 2019, pp. 1863–1867.
[7] B. Gerazov and R. C. Conceicao, "Deep learning for tumour classification in homogeneous breast tissue in medical microwave imaging," in *Proc. IEEE 17th Int. Conf. Smart Technol.*, 2017, pp. 564–569.
[8] S. P. Rana et al., "Machine learning approaches for automated Lesion detection in microwave breast imaging clinical data," *Sci Rep.*, vol. 9, no. 1, pp. 1–12, Jul. 2019.
[9] T. Reimer and S. Pistorius, "The diagnostic performance of machine learning in breast microwave sensing on an experimental dataset," *IEEE J. Electromagn., RF, Microw. Med. Biol.*, vol. 6, no. 1, pp. 139–145, Mar. 2022.
[10] V. Suresh and R. Kiran, "3D inverse electromagnetic solver using deep neural network towards breast cancer detection," in *Proc. IEEE Recent Adv. Intell. Comput. Syst.*, 2018, pp. 214–218.
[11] F. Abujarad, A. Jostingmeier, and A. S. Omar, "Clutter removal for landmine using different signal processing techniques," in *Proc. IEEE 10th Int. Conf. Ground Penetrating Radar*, 2004, pp. 697–700.
[12] W. Zhi and F. Chin, "Entropy-based time window for artifact removal in UWB imaging of breast cancer detection," *IEEE Signal Process. Lett.*, vol. 13, no. 10, pp. 585–588, Oct. 2006.
[13] H. Song et al., "A two-stage rotational surface clutter suppression method for microwave breast imaging with multistatic impulse-radar detector," *IEEE Trans. Instrum. Meas.*, vol. 69, no. 12, pp. 9586–9598, Dec. 2020.
[14] K. Noritake and S. Kidera, "Surface clutter suppression with FDTD recovery signal for microwave UWB mammography," *IEICE Trans. Elecron.*, vol. E103-C, no. 1, pp. 9586–9598, Jan. 2020.
[15] H. Ma, S. Sasada, M. Okada, T. Kikkawa, and S. Kidera, "Clinical test of surface rejection method for microwave breast cancer imaging," in *Proc. IEEE USNC-URSI Radio Sci. Meeting (Joint With AP-S Symp.)*, 2021, pp. 43–44.
[16] H. Song et al., "Detectability of breast tumor by a hand-held impulse-radar detector: Performance evaluation and pilot clinical study," *Sci. Rep.*, vol. 7, Nov. 2017, Art. no. 16353.
[17] U. Hirose, P. Zhu, and S. Kidera, "Deep learning enhanced contrast source inversion for microwave breast cancer imaging modality," *IEEE J. Electromagn., RF, Microw. Med. Biol.*, vol. 6, no. 3, pp. 373–379, Sep. 2022.

Peixian Zhu (Graduate Student Member, IEEE) received the B.E. degree in automation engineering from the Shandong University of Technology, Zibo, China, in 2018, and the M.E. degree from the Graduate School of Informatics and Engineering, University of Electro-Communications, Tokyo, Japan, in 2022, where he is currently working toward the D.E. degree with the Graduate School of Informatics and Engineering. His research interests include electromagnetic tomography and its applications.

Shouhei Kidera (Senior Member, IEEE) received the B.E. degree in electrical and electronic engineering and the M.I. and Ph.D. degrees in informatics from Kyoto University, Kyoto, Japan, in 2003, 2005, and 2007, respectively. In 2009, he joined as an Assistant Professor with the University of Electro-Communications, Tokyo, Japan. He is currently a full Professor with the Graduate School of Informatics and Engineering, University of Electro-Communications. he was a Visiting Researcher with the Cross-Disciplinary Electromagnetics Laboratory, University of Wisconsin Madison, Madison, WI, USA. From 2017 to 2021, he has been a Principal Investigator of the PRESTO Program of Japan Science and Technology Agency. His research interests include advanced radar signal processing, electromagnetic inverse scattering issue for ultra wideband three-dimensional sensor, and bio-medical applications. In 2016, he was the recipient of the 2012 Ando Incentive Prize for the Study of Electronics, 2013 Young Scientist's Prize by the Japanese Minister of Education, Culture, Sports, Science and Technology (MEXT), 2014 Funai Achievement Award, 2022 KDDI Foundation Award, Contribution Award, and 2023 RIEC Award. He is a Senior Member of the Institute of Electronics, Information, and Communication Engineers of Japan, and International Union of Radio Science (Union Radio-Scientifique Internationale, URSI), and a Member of the Institute of Electrical Engineering of Japan and Japan Society of Applied Physics.

Authorized licensed use limited to: UNIVERSITY OF ELECTRO COMMUNICATIONS. Downloaded on May 23,2025 at 13:13:21 UTC from IEEE Xplore. Restrictions apply.